# Evaluation of Push-Pull manoeuvring mode for a naval ship using CFD

Gyeongseo Min[1], Wooseok Choi[1], Haechan Yun[1], Younguk Do[1], Kangmin Kim[1], Momchil Terziev[2], Saishuai Dai[2], Daejeong Kim[3], Soonseok Song*[1]

*corresponding author email: s.song@inha.ac.kr

[1]Department of Naval Architecture & Ocean Engineering, Inha University, Republic of Korea

[2]Department of Naval Architecture, Ocean and Marine Engineering, University of Strathclyde, United Kingdom

[3]Division of Navigation Convergence Studies, Korea Maritime & Ocean University, Republic of Korea

## Abstract

Enhanced manoeuvring capabilities are critical for modern warships, as they directly impact mission success and defensive operations. Various strategies have been proposed to improve a ship's manoeuvrability, including the use of bilge keels and fin stabilizers. This study investigates the application of the Push-Pull mode—a manoeuvring technique that uses both pushing and pulling propellers—as a potential means to enhance overall manoeuvring performance. While this mode is typically employed in docking operations, its effectiveness in general manoeuvring scenarios remains largely unexplored. To assess its impact, a free-running manoeuvre model for the fully appended Office of Naval Research Tumblehome (ONRT) hull was developed using the Unsteady Reynolds-Averaged Navier-Stokes (URANS) method. The ship's performance was evaluated through both turning circle and U-turn (turning back) manoeuvres under two configurations: Push-Pull mode and the conventional rudder-only method. Simulation results demonstrated that the Push-Pull mode significantly enhanced manoeuvrability in both manoeuvre types, indicating its potential applicability beyond docking scenarios.

Keywords: Computational Fluid Dynamics, manoeuvrability, free running simulation, Push-Pull mode, Turning back (U-turn),

## 1. Introduction

The manoeuvrability of ships is an important factor for both safety and operational efficiency. From a safety perspective, ships with good manoeuvrability can swiftly alter their course avoiding collisions and other hazards, enabling rapid and controlled emergency responses. In terms of operations, ships frequently subjected to external environmental factors such as wind, waves, and currents. Vessels with superior manoeuvring capabilities can more effectively adjust their course to counter these factors, thereby minimising unnecessary fuel consumption and ultimately enhancing overall efficiency.

Several manoeuvrability performance criteria are used to evaluate a ship's manoeuvrability, including course-keeping ability, turning ability, course-changing ability, and stopping ability. These criteria are assessed through standardised tests. Course-keeping ability is evaluated using the spiral test, which determines the ship's directional stability by measuring its response to incremental rudder angle changes. Turning ability is assessed through the turning circle test, where the ship executes a full turn at a constant rudder angle, and key parameters such as tactical diameter and advance are measured. Course-changing ability is evaluated through the zigzag test, which involves alternating rudder inputs to assess the ship's responsiveness in changing course. Stopping ability is measured through the stopping manoeuvre, where the propeller is reversed, and both the stopping distance and time to achieve a full stop are recorded.

These manoeuvrability criteria are evaluated by various methods. The traditional method is through experiments. Experiments are conducted by manufacturing model ships and testing them in model basins. This method has provided reliable results over a long period of time (Yasukawa & Faizul, 2006; Yoshimura et al., 2008). Recently, the manoeuvrability of the Office of Naval Research Tumblehome (ONRT) surface combatant model in waves was assessed through experiments (Sanada et al., 2018). The model tests were carried out under calm water and various wave conditions in the IIHR wave basin. Similarly, a free-running model test of the KVLCC2 model ship in waves was carried out in the KRISO Ocean Engineering basin (Kim et al., 2019).

However, the improvement of computing power has led to advancements in Computational Fluid Dynamics (CFD). As a result, using CFD has become one of the methods to estimate the manoeuvring performance. There have been various studies have utilised CFD to assess the manoeuvrability of ships (Carrica et al., 2016; Hasanvand et al., 2019; Wang & Wan, 2020; Wang et al., 2017). For instance, the effect of metacentric height (GM) on ship manoeuvring characteristics was demonstrated using CFD (Song et al., 2024). Simulation results under various GM conditions showed that a reduction in GM increased overshoot angles during zigzag manoeuvres by influencing roll motion. Additionally, a small GM leads to a shrinking turning trajectory due to excessive speed reduction caused by increased roll motion during turning manoeuvres. In another study, the influence of sudden propulsion loss on ship operation in various wave heights was assessed (Kim et al., 2022). It was found that the length of the ship's advance during turning performance under identical wave heights increased under propulsion loss conditions compared to normal operation. Furthermore, the effects of damaged compartments on turning manoeuvres were studied using a free-running CFD method (Dong et al., 2023). The study revealed that the damaged ship exhibited a smaller turning circle along with larger roll, pitch, and heave motions compared to the intact ship. As outlined above, various studies have been conducted on ship manoeuvring performance through CFD.

In this context, manoeuvrability is an especially important topic in naval ships. The first reason for this is the survivability of warships. Warships often face situations where they need to evade enemy attacks, including missiles, torpedoes, and other threats during combat. Enhanced manoeuvrability increases survivability by ensuring a higher probability of avoiding attacks. The second reason is operational effectiveness. Naval ships are required to conduct complex tactical manoeuvres to carry out missions. In this aspect, superior manoeuvrability enables them to perform these manoeuvres effectively. Then, how can the manoeuvrability of warships be improved? According to the author, the answer to this question lies in integrating the Push-Pull mode into the operation of the ship.

The Push-Pull mode refers to a manoeuvring technique where one main propeller operates astern at maximum power while the other runs ahead, balancing the longitudinal force at a desired level and generating a high transverse force and yaw moment. Ships usually use the Push-Pull mode for berthing or unberthing. In an earlier study, the Push-Pull mode was investigated by varying the distance between the hull and the side quay during captive model tests (Yoo et al., 2006). It was found that the flow of the reverse propeller, induced from the stern to the bow, creates a channel flow between the hull and the side quay in restricted water during the Push-Pull mode. Consequently, the bank suction effect develops, which hinders unberthing motion. Similarly, a mathematical model of motion and controller was constructed for the crabbing motion using the Push-Pull mode (Park & Kim, 2013). It was validated by simulation for both auto-berthing situations and unberthing situations, confirming the effectiveness of the control algorithm.

Recently, the development of electric propulsion ships has led to an increase in the operational flexibility of a ship's propeller. As a result, incorporating propulsion mode changes, such as the Push-Pull mode, into the operation of the ship could be an effective approach to enhancing manoeuvrability. However, to the best of the author's knowledge, there has been no specific study that estimates manoeuvring performance using the Push-Pull mode with CFD. In this context, the question arises as to how applying the Push-Pull mode to warships, where manoeuvring performance is critical, might affect their manoeuvring performance. Therefore, this study aims to address this question by developing a CFD model to predict variations in the manoeuvring performance when the Push-Pull mode is used on naval ships. In this paper, a free-running manoeuvre model was developed to estimate the manoeuvring performance of warships under various Push-Pull modes through CFD. Specifically, manoeuvre conditions were considered where the propeller could either be off or in reverse, and the rudder could either be moving or stationary. These four combinations of propeller and rudder conditions were examined under different Push-Pull modes to estimate manoeuvring performance.

This paper is organised as follows: The methodology of the present study is described in Section 2, which includes specific details on the mathematical formulations, geometry, boundary conditions, and mesh generation. Section 3 presents the spatial and temporal verification studies, as well as validation studies against experimental data. Section 4 is divided into two parts. The first part discusses the ‘turning-circle’ simulations under various Push-Pull modes, while the second part presents the results of ‘U-turn’ simulations under different Push-Pull modes. The length of advance, transfer, and tactical diameter for each scenario was estimated to compare manoeuvring performance.

## 2. Methodology

### 2.1. Mathematical formulations

A free running manoeuvring model was developed by using a commercial CFD software package, STAR-CCM+ (version 19.04.009), based on the unsteady Reynolds-averaged Navier-Stokes (URANS) method. The following two equations express the averaged continuity and momentum equations for incompressible flows in tensor notation and Cartesian coordinates (Ferziger et al., 2019).

$$\frac{\partial(\rho\overline{u_i})}{\partial\overline{x_i}} = 0 \tag{1}$$

$$\frac{\partial(\rho\overline{u_i})}{\partial t} + \frac{\partial}{\partial x_j}\left(\rho\overline{u_i}\overline{u_j} + \rho\overline{u_i'u_j'}\right) = -\frac{\partial\bar{p}}{\partial x_i} + \frac{\partial\overline{\tau_{ij}}}{\partial x_i} \tag{2}$$

where, $\rho$ denotes the fluid density, $\overline{u_i}$ denotes the averaged velocity vector, $\rho\overline{u_i'u_j'}$ denotes the Reynolds stress, $\bar{p}$ denotes the averaged pressure, and $\partial\overline{\tau_{ij}}$ denotes the mean viscous stress tensor components. This viscous stress for a Newtonian fluid can be expressed as

$$\overline{\tau_{ij}} = \mu\left(\frac{\partial\overline{u_i}}{\partial x_j} + \frac{\partial\overline{u_j}}{\partial x_i}\right) \tag{3}$$

in which, $\mu$ denotes the dynamic viscosity.

Using the Boussinesq hypothesis, the Reynolds stress can be written as

$$-\rho\overline{u_i'u_j'} = \mu_t\left(\frac{\partial\overline{u_i}}{\partial x_j} + \frac{\partial\overline{u_j}}{\partial x_i}\right) - \frac{2}{3}\left(\rho k + \mu_t\frac{\partial\overline{u_k}}{\partial x_k}\right)\delta_{ij} \tag{4}$$

in which, $\mu_t$ denotes the turbulent eddy viscosity, $k$ denotes the turbulent kinetic energy, and $\delta_{ij}$ denotes the Kronecker delta.

In the CFD solver, the computational domain was discretised and the governing equations were solved using the Finite Volume Method (FVM). For the momentum equations, the second-order upwind convection scheme and a first-order temporal discretisation were applied. The overall solution procedure employed an algorithm of the Semi-Implicit Method for Pressure-Linked Equations (SIMPLE) type.

In this study, the shear stress transport (SST) $k-\omega$ turbulence model was used to account for the effects of turbulence. The SST $k-\omega$ turbulence model incorporates the advantages of the $k-\omega$ and $k-\varepsilon$ turbulence models. It uses a $k-\omega$ formulation in the inner regions of the boundary layer and a $k-\varepsilon$ formulation in the free-stream. This approach provides more accurate near wall treatment and reduces sensitivity to the properties of inlet turbulence. These characteristics lead to a better prediction in adverse pressure gradients and separating flow. Moreover, the Volume of Fluid method was employed with the High Resolution Interface Capturing (HRIC) to capture the free surface.

To reduce computational cost, the body-force propeller method was used to represent the characteristics of the propeller. The body-force propeller method calculates the effects on the flow from the axial and tangential forces of the modelled propeller. Subsequently, the thrust and torque are obtained by integrating these forces over the disk and are treated as body force terms in the governing equations (D. Kim et al., 2021). Applying this method,

instead of modelling the rotating propeller in the free running simulations, reduces computation time. Moreover, this method has been proven effective through a previous study (I.-T. Kim et al., 2021).

## 2.2. Geometry and boundary conditions

Table 1 and Fig. 1 represent the geometry and the principal particulars of the model-scale ONRT used in this study. The ONRT model ship has the twin rudders and twin propellers, making it suitable for evaluating the Push-Pull mode. The scale factor of 48.935 was selected to enable a comparison between the simulation results and the experimental data of IIHR provided by the SIMMAN 2020 workshop.

**Fig. 1.** Geometry of ONRT hull with rudders

**Table 1** The principal particulars of the ONRT model used in this study

| Main particulars | Symbols | Models scale |
|---|---|---|
| Scale factor | $\lambda$ | 48.935 |
| Length of waterline | $L_{WL}$ (m) | 3.147 |
| Maximum beam of waterline | $B_{WL}$ (m) | 0.384 |
| Depth | $D$ (m) | 0.266 |
| Draft | $T$ (m) | 0.112 |
| Displacement | $\Delta$ (kg) | 72.6 |
| Wetted surface area (fully appended) | $S_0$ $(m^2)$ | 1.5 |
| Block coefficient | $C_B$ | 0.535 |
| Metacentric height | GM (m) | 0.0422 |
| Radius of gyration for roll | $k_{xx}/B$ | 0.344 |
| Radius of gyration for yaw | $k_{zz}/L_{pp}$ | 0.246 |
| Froude number | $F_n$ | 0.2 |
| Approach speed | $U_0$ (m/s) | 1.11 |
| Propeller diameter | $D_p$ (m) | 0.1066 |
| Propeller rotation direction (view from stern) | | inward |
| Maximum rudder rate | (deg/s) | 35.0 |

Fig. 2 illustrates the computational domain and the respective boundary conditions. Moreover, Fig. 3 depicts the multi-level dynamic overset grid system for the background, hull, and rudders. The background domain was modelled to follow the ship's three degrees of freedom (3-DOF) motions (i.e., surge, sway, and yaw), while the hull overset domains move in six degrees of freedom (6-DOF) motions. The two rudder overset domains move within the hull overset domains, superposing the rudder's motion onto the hull's motion.

The Propeller Open Water (POW) data were needed to use the body-force propeller method. Therefore, to implement the Push-Pull mode, open water test results for a reverse rotating propeller were required. However, the experimental data for the reverse rotating propeller were not available. For this reason, simulations of the reverse rotating propeller to acquire open water test data were conducted beforehand. The computational domain and boundary conditions for these simulations are shown in Fig. 4. The MRF approach, known as the 'Multiple Reference Frame', was applied to these simulations for the POW test. This approach is a steady-state approximation method, which requires less computational power compared to unsteady methods (e.g. the Sliding mesh). Nevertheless, the results obtained using the MRF approach were found to be in good agreement with those from unsteady methods. This has been confirmed by previous studies (Machado & Fernandes, 2021; Song et al., 2019; Song et al., 2020).

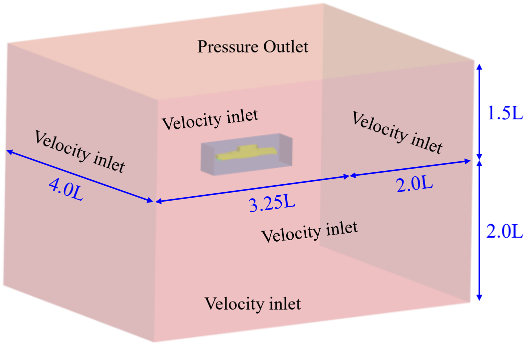


**Fig. 2.** Computational domain and boundary conditions of free running simulations

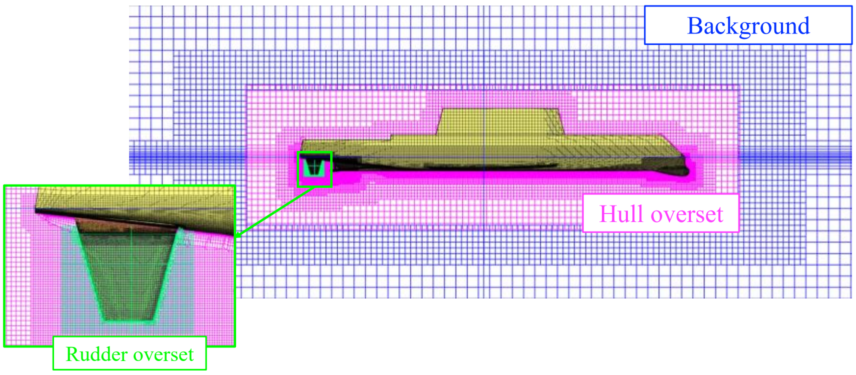


**Fig. 3.** Multi-level overset grid system for background, hull, and rudders

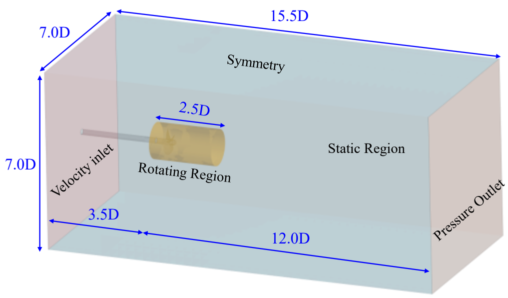


**Fig. 4.** Computational domain and boundary conditions of propeller open water tests

## 2.3. Mesh generation

The trimmed cell meshes with prism layers were generated using the built-in meshing tool of STAR-CCM+ (version 19.04.009). The grid system of free running simulations is illustrated in Fig. 5. Specifically, local mesh refinements were applied to significant regions for numerical calculations. In the free running simulation, mesh refinements were added to capture the waves which are generated by hull and to refine the mesh near the rudder. The wall $y^+$ values were set to be less than 1 for all the hull and rudder surfaces by adjusting the thickness of the first layer cell in these simulations.

In the case of POW test simulations, the grid system is presented in Fig. 6. In these simulations, mesh refinements were applied to propeller tips and hub to improve numerical accuracy. As in the free running simulation, the wall $y^+$ values were set to be below 1 by defining an appropriate first layer cell thickness.

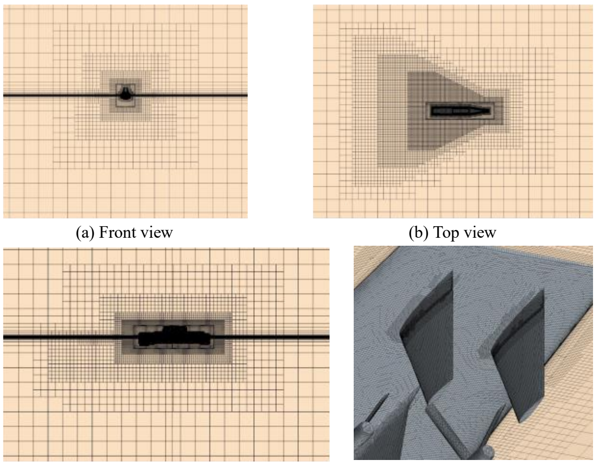

(a) Front view (b) Top view

(C) Side view (D) Mesh refinement of rudder

**Fig. 5.** Grid system of free running simulation

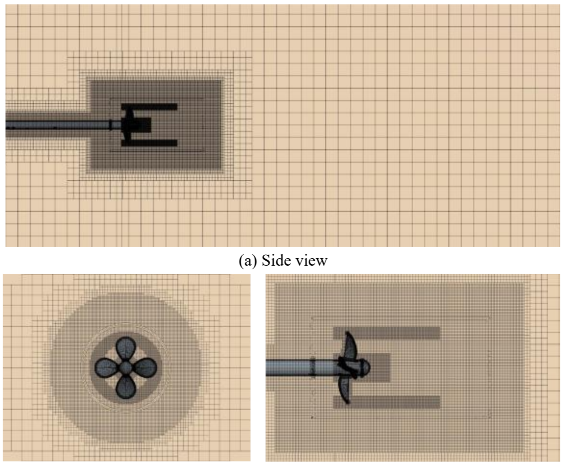

(a) Side view

(b) Front view (C) Mesh refinement

**Fig. 6.** Grid system of propeller open water test simulation

## 2.4. Controllers

Before executing zigzag, turning, and Push-Pull manoeuvres, the ship needs to be in a self-propelled state with a zero heading angle. Therefore, in this study, a Proportional-Integral (PI) controller was applied to the propeller and a Proportional-Integral-Differential (PID) controller was applied to the rudder to achieve that state.

### 2.4.1. Propeller controller

The Revolution Per Second (RPS) of the propeller is adjusted by the PI controller to reach the target speed. The PI controller used in this study is as follows.

$$n = n_0(1 + K_{P,Prop} e_{speed} + K_{I,Prop} \int_0^t e_{speed}\, dt) \quad (5)$$

In this equation, $n$ represents the rotational speed of the propeller, $n_0$ represents the initial rotational speed of the propeller, and $K_{P,prop}$ and $K_{I,prop}$ represent the proportional and integral control gains. In this context, $e_{speed}$ is defined as follows.

$$e_{speed} = V_{target} - V_{ship} \quad (6)$$

In the following equation, $V_{target}$ is set to 1.11 m/s, which matches the experimental data, and $V_{ship}$ is the speed of the ship. The control gains used in this controller were set to $K_{P,prop} = 1/V_{target}$ and $K_{I,prop} = 1.2/L_{pp}$. Fig. 7 illustrates the time history of the propeller rotation speed and ship speed using this PI controller, until the self-propulsion state is achieved. As a result, the rotational speed of the numerical simulation is 9.16 rps, which shows only a slight difference compared to the experimental results from IIHR, where the rps is 8.97 (Sanada et al., 2018). After achieving a self-propelled state, the zigzag, turning, and Push-Pull manoeuvre are conducted with the constant rotational speed determined through the numerical simulation.

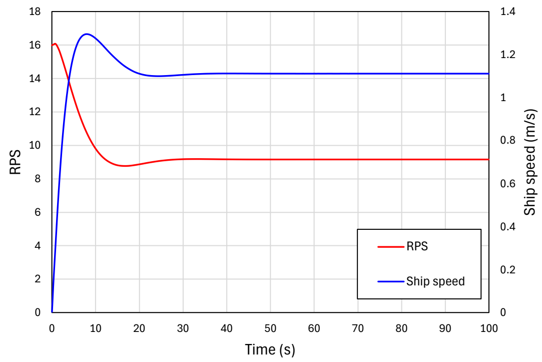


**Fig. 7.** Time history of the propeller rotation speed and ship speed until achieving self-propulsion

### 2.4.2. Rudder controller

To achieve a self-propelled state with a zero heading angle, the neutral rudder angle needs to be determined. Therefore, a PID controller was applied to the rudder and used together with a PI controller on the propeller. The equation for the PID controller implemented on the rudder is as follows.

$$\delta_N = K_{P,rud} e_\psi + K_{I,rud} \int_0^t e_\psi\, dt + K_{D,rud} \dot{e_\psi} \quad (7)$$

In this equation, $\delta_N$ denotes the neutral rudder angle, $K_{P,rud}$ denotes the proportional gain, $K_{I,rud}$ denotes the integral gain, and $K_{D,rud}$ denotes the differential gain. Additionally, $e_\psi$ is the heading angle error defined as,

$$e_\psi = \psi_{target} - \psi \quad (8)$$

In this context, $\psi$ is the heading angle and $\psi_{target}$ is set to zero to maintain alignment with the desired heading angle. The control gains were set to $K_{P,rud} = 1$, $K_{I,rud} = 0.6\, V_{target}/L_{pp}$, and $K_{D,rud} = L_{pp}/V_{target}$. The results of the time history of rudder and heading angle until achieving self-propelled state are shown in Fig. 8. According to the simulation results, the zero heading angle is achieved with the neutral rudder angle at 0.097°. In the zigzag, turning, and Push-Pull manoeuvres, the rudders were controlled at each condition without exceeding the maximum rudder rate, adjusting to the appropriate angles for each manoeuvre.

In both the propeller controller and rudder controller, the values of the control gain did not affect the numerical results. However, the selected control gains were intended for efficient manoeuvring simulations to reduce computational time.

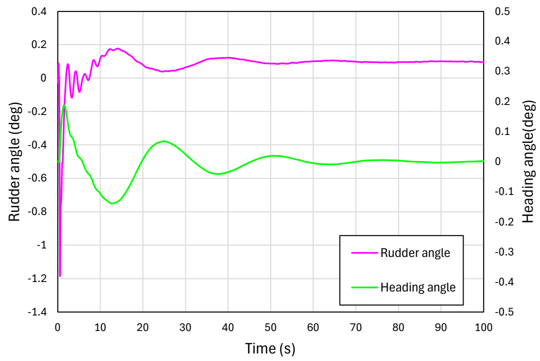


**Fig. 8.** Time history of the rudder angel and heading angle until achieving self-propulsion

## 2.5. Operating conditions of Push-Pull mode

### 2.5.1. Conditions of Push-Pull mode during turning circle manoeuvre

The performance of turning circle and turning back (i.e. U-turn) manoeuvres under various Push-Pull modes is estimated through CFD in this paper. To first examine the conditions of the Push-Pull modes for the turning circle manoeuvre, the Push-Pull mode conditions involve either keeping the Portside rudder fixed or turning it to 35 degrees, as well as either turning off or reversing the rotation of the Portside propeller. Table 2 outlines these various operational conditions of the Push-Pull mode. As presented in Table 2, the rotational speed of the propeller represents the full-scale rpm, and the rotational speed of the reverse rotating propeller is expressed as negative for the convenience of understanding. Additionally, the direction of the forces acting on the ship due to the thrust generated by the propeller, as well as the appearance of the rudder in each case, are depicted in Fig. 9. Specifically, Cases 1 and 3 feature asymmetric rudder conditions, while Cases 2 and 4 have symmetric rudder conditions, as shown in Fig. 9. Furthermore, Cases 1 and 2 include scenarios with the propeller turned off, whereas Cases 3 and 4 correspond to conditions with the propeller rotating in reverse. These conditions are compared to the traditional turning method, defined as the Base case, which relies solely on rudder usage.

**Table 2** Different operation conditions of Push-Pull mode during turning circle manoeuvre

| | Description | Propeller direction. PS | Propeller direction. SB | PS. Propeller | SB. Propeller | PS. Rudder | SB. Rudder |
|---|---|---|---|---|---|---|---|
| Base | Fwd/Fwd/35°/35° | Forward | Forward | 78.57 rpm | 78.57 rpm | 35 deg | 35 deg |
| Case 1 | Off/Fwd/0°/35° | Off | Forward | 0 | 78.57 rpm | 0 deg | 35 deg |
| Case 2 | Off/Fwd/35°/35° | Off | Forward | 0 | 78.57 rpm | 35 deg | 35 deg |
| Case 3 | Rev/Fwd/0°/35° | Reverse | Forward | -78.57 rpm | 78.57 rpm | 0 deg | 35 deg |
| Case 4 | Rev/Fwd/35°/35° | Reverse | Forward | -78.57 rpm | 78.57 rpm | 35 deg | 35 deg |

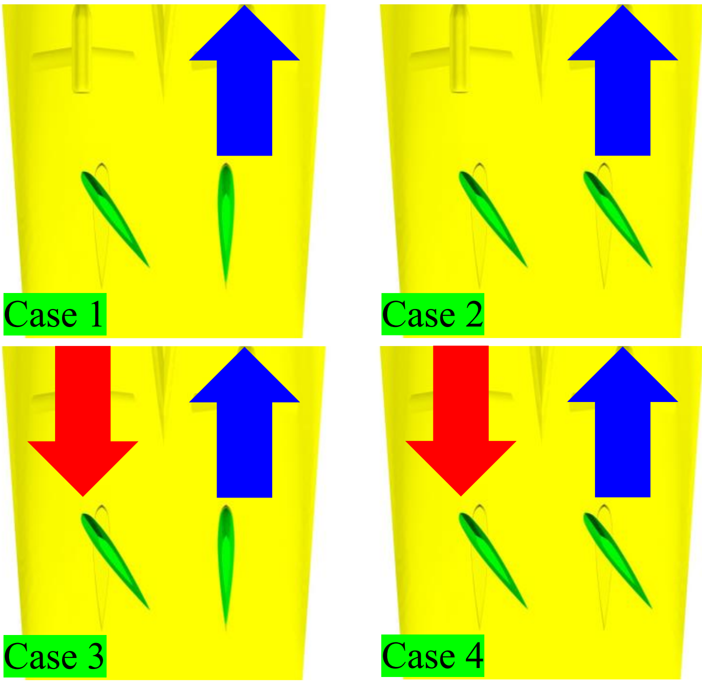


**Fig. 9.** A schematic representation of the Push-Pull mode conditions

In Push-Pull mode, the control of the ship's rudder and propeller is performed simultaneously. For conditions involving a reverse rotating propeller, such as in Case 2 and Case 4, the forward rotating propeller gradually powers down before the propeller begins operating in reverse rotation. When the rudder angle reaches 35 degrees, the reverse rotating propeller is controlled to rotate in the opposite direction at the same rotational speed as the Starboard propeller, which is the rotational speed in the self-propeller state. In conditions where the propeller is turned off such as in Case 1 and Case 3, the Portside propeller is turned off at the same rate as when the reverse rotating propeller is operating in Case 2 and Case 4. The specific propeller controller in Push-Pull mode is represented in Equation 9. In this equation, $n_{PS}$ denotes the rotation speed of the Portside propeller, $\delta$ denotes the rudder angle, and $n_{fix}$ denotes the fixed rotation speed of Starboard propeller.

$$n_{PS} = \begin{cases} n_{fix}\ (\delta < 0) \\ -\frac{2\times n_{fix}}{35}\delta + n_{fix}\ \ (0 \leq \delta < 35) \\ -n_{fix}\ (\delta \geq 35) \end{cases} \tag{9}$$

Fig. 10 and Fig. 11 illustrate the time history of the rudder angle and the rotational speed of the propeller in Push-Pull mode using this controller. Furthermore, the flow under the hull for each case is represented in Fig. 12. As shown in Fig. 12, there is an absence of flow entering through the Portside propeller under the off propeller condition in Cases 1 and 2. However, the flow through the Portside propeller is observed to reverse under the reverse rotating condition in Cases 3 and 4.

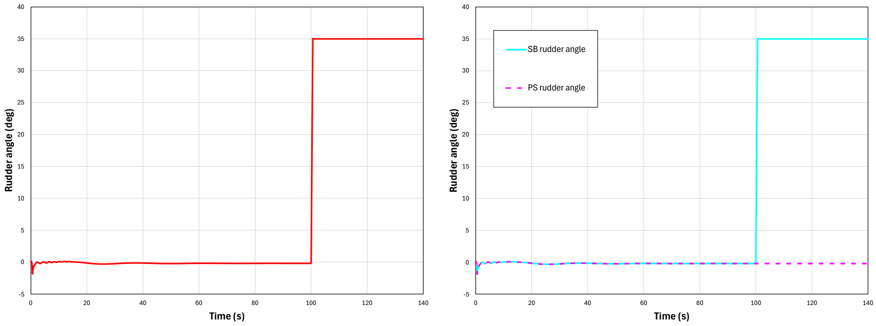


(a) Symmetric rudder condition (b) Asymmetric rudder condition

**Fig. 10.** Time history of rudder angle in Push-Pull mode during turning circle manoeuvre

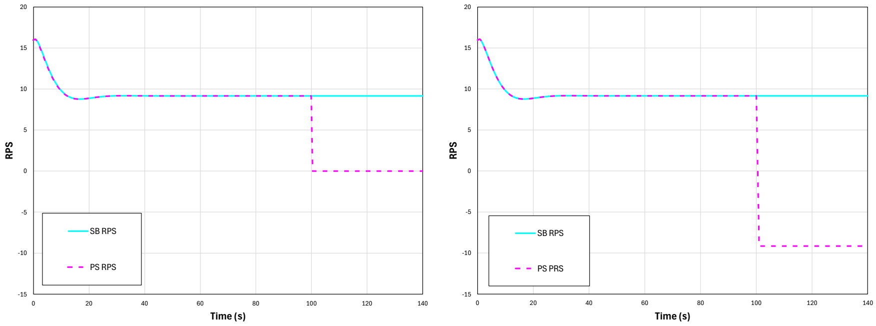


(a) Off propeller condition (b) Reverse propeller condition

**Fig. 11.** Time history of rotational speed of propeller in Push-Pull mode during turning circle manoeuvre

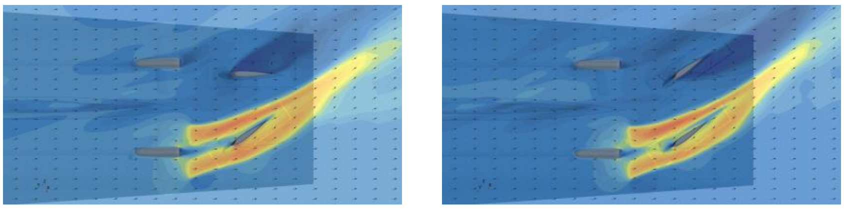

(a) Case 1: Off/Forward/0°/35° (b) Case 2: Off/Forward/35°/35°

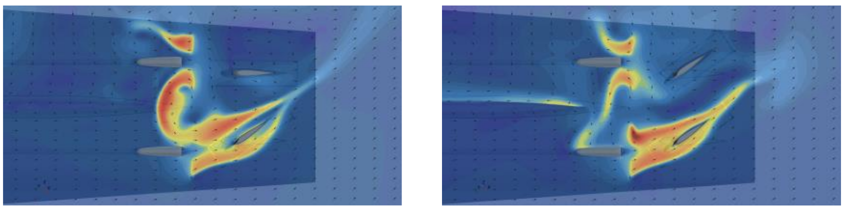

(c) Case 3: Reverse/Forward/0°/35° (d) Case 4: Reverse/Forward/35°/35°

**Fig. 12.** Flow under the hull in different Push-Pull mode

### 2.5.2. Conditions of Push-Pull mode during turning back manoeuvre

Moreover, turning back manoeuvre (i.e. U-turn) simulations were conducted in this paper to better reflect actual operational conditions. In these simulations, a Proportional-Differential (PD) controller was used to control the rudder for turning 180 degrees after achieving the self-propelled state. The equation for the PD controller is as follows.

$$\delta_U = K_{P,rud} e_U + K_{D,rud} \dot{e_U} \tag{10}$$

$$e_U = \psi_U - \psi \tag{11}$$

In these equations, $\delta_U$ denotes the rudder angle for the turning back manoeuvre, while $K_{P,rud}$ and $K_{D,rud}$ represent the proportional and differential control gains. Additionally, these control gains are the same as those used to achieve the self-propulsion state. However, the error was defined differently. In this equation, $e_U$ is the heading angle error for the turning back manoeuvre, $\psi_U$ is set to 180°, and $\psi$ is the heading angle. The time histories of the rudder and heading angle during the turning back manoeuvre using this controller are represented in Fig. 13. Additionally, this PD controller is also applied in the turning back simulations using the Push-Pull mode.

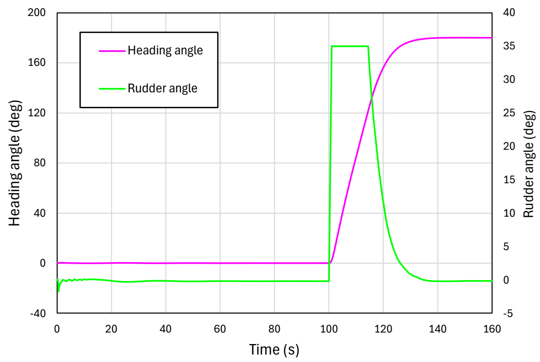


**Fig. 13.** Time histories of the rudder and heading angle during turning back manoeuvre

Before undertaking turning back manoeuvres with various Push-Pull modes, a turning back simulation based on the traditional rudder method was conducted to establish the reference standard for comparison. Similar to the turning circle simulation, this simulation was carried out with a constant rotational speed of the propeller, which achieves the self-propelled state. The results of trajectory, surge speed, and roll angle from this simulation are illustrated in Fig. 14 and Fig. 15. These serve as a basis for comparison with those obtained using the Push-Pull mode.

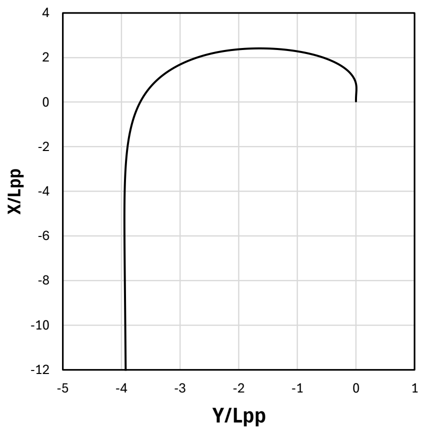


**Fig. 14.** Trajectory of the turning back manoeuvre

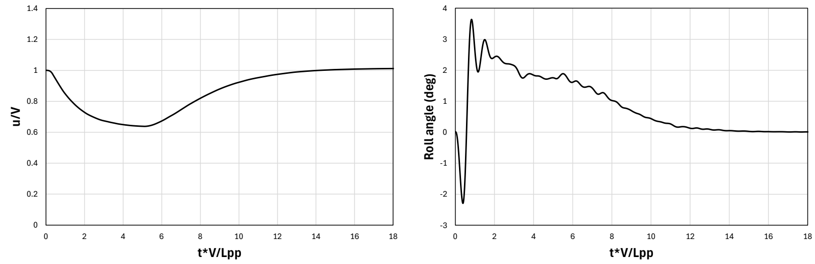


(a) Surge speed during the turning back manoeuvre

(b) Roll angle during the turning back manoeuvre

**Fig. 15.** Surge speed and roll angle during turning back manoeuvre

Table 3 indicates various operating conditions of Push-Pull mode during the turning back manoeuvre. As presented in Table 3, the operating states in Push-Pull mode during the turning back manoeuvre are the same as those during the turning circle manoeuvre. Furthermore, the control of propeller's rotational speed is governed in the same way as in the turning circle manoeuvre, depending on the rudder angle. However, as shown in Fig. 13, the rudder angle changes during turning back manoeuvre unless fixed to zero degrees under an asymmetric rudder condition. Therefore, the rotational speed of Portside propeller changes with the rudder angle. Specifically, Fig. 16 depicts how the rotational speed of the Portside propeller varies during turning back manoeuvre.

**Table 3** Different operation conditions of Push-Pull mode during turning back manoeuvre

| | Description | Propeller direction. PS | Propeller direction. SB | Min. PS. Propeller | SB. Propeller | Max. PS. Rudder | Max. SB. Rudder |
|---|---|---|---|---|---|---|---|
| Base | Fwd/Fwd/35°/35° | Forward | Forward | 78.57 rpm | 78.57 rpm | 35 deg | 35 deg |
| Case 1 | Off/Fwd/0°/35° | Off | Forward | 0 | 78.57 rpm | 0 deg | 35 deg |
| Case 2 | Off/Fwd/35°/35° | Off | Forward | 0 | 78.57 rpm | 35 deg | 35 deg |
| Case 3 | Rev/Fwd/0°/35° | Reverse | Forward | -78.57 rpm | 78.57 rpm | 0 deg | 35 deg |
| Case 4 | Rev/Fwd/35°/35° | Reverse | Forward | -78.57 rpm | 78.57 rpm | 35 deg | 35 deg |

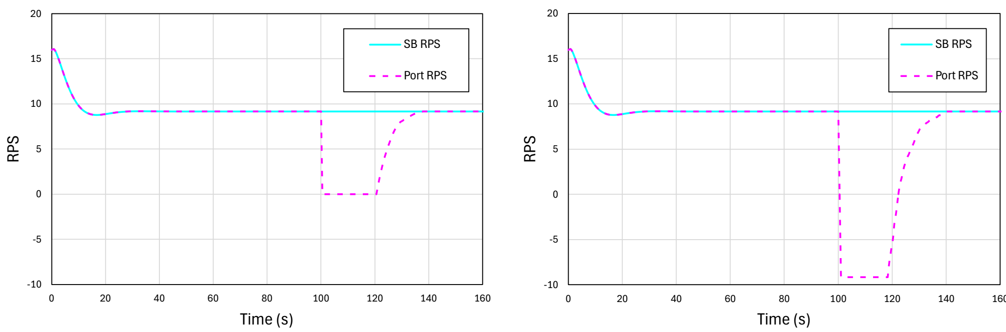


(a) Off propeller condition

(b) Reverse propeller condition

**Fig. 16.** Time history of rotational speed of propeller in Push-Pull mode during turning back manoeuvre. (a) Off propeller condition was applied to Cases 1 and 2, and (b) Reverse propeller condition was applied to Cases 3 and 4.

# 3. Validation and Verification

## 3.1. Validation against EFD

The validation studies are divided into two parts. The first part compares the CFD results with the experimental data of the POW tests, as discussed in Section 3.1.1. The second part presents a comparison between the CFD and EFD results for the free running manoeuvres, detailed in Section 3.1.2 and Section 3.1.3.

### 3.1.1. Propeller open water test

Before the POW test for reverse rotation, simulations for the forward rotating propeller were conducted to compare the experimental results. The experimental data were provided by IIHR for the SIMMAN 2020 workshop. As shown in Fig. 9a, a good agreement was achieved between the experimental and CFD results, with only a slight overestimation of torque and thrust in the CFD compared to the experiment.

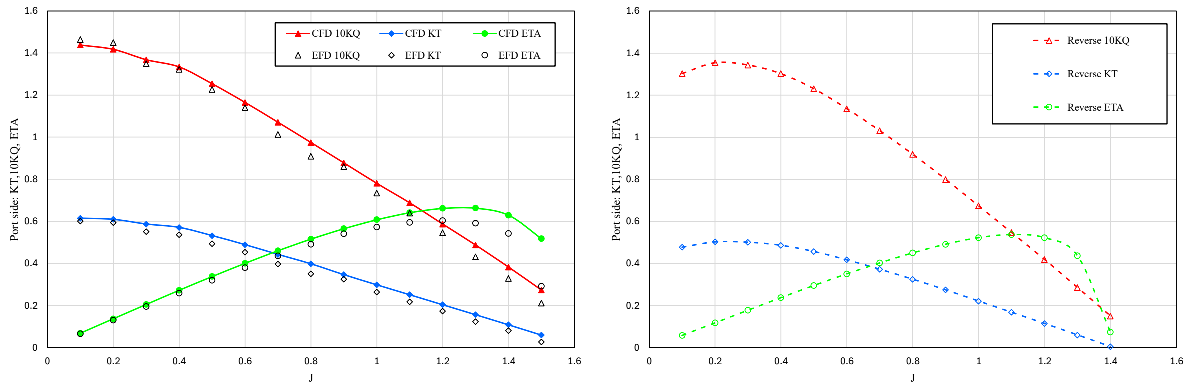


(a) Open water curve of forward rotating propeller

(b) Open water curve of reverse rotating propeller

**Fig. 17.** Comparison of the propeller open water curves obtained from the experiment and CFD

After confirming that the results of the forward rotating propeller were in good agreement with the experiment, the simulations of the reverse rotating propeller simulations were carried out. Fig. 9b represents the results of POW test under reverse rotating condition. As shown in Fig. 9b, thrust, torque, and efficiency of the propeller decrease across the entire range of the advance ratio in reverse rotating condition. Subsequently, the propeller open water curves of the reverse rotating propeller were used in the Push-Pull mode for the body-force propeller method.

### 3.1.2. 35° Portside turning circle manoeuvre

For the validation of the free running simulations, the results of the 35° Portside turning circle manoeuvre and 20°/20° zigzag manoeuvre were evaluated against the experimental data provided by IIHR as part of the SIMMAN 2020 workshop. In the case of the 35° Portside turning manoeuvre, the trajectories obtained from the CFD and EFD are compared in Fig. 18. Moreover, Fig. 19 presents a comparison of surge speed and roll angle between the CFD and EFD results during the 35° Portside turning circle manoeuvre. For the results of trajectories, surge speed, and roll angle derived from CFD show good agreement with experimental results. Specifically, the differences between the turning circle manoeuvre characteristics obtained from the CFD and EFD are presented in Table 4. There is a slight difference between the CFD and EFD, but the discrepancies are minor and the author believes that these discrepancies do not significantly affect the results of the present study.

**Table 4** Comparison of the turning circle manoeuvre characteristics obtained from CFD and EFD

| | CFD | EFD (IIHR) | Difference |
|---|---|---|---|
| Transfer/$L_{pp}$ | 1.258 | 1.305 | 3.60% |
| Advance/$L_{pp}$ | 2.361 | 2.325 | 1.55% |
| Tactical Diameter/$L_{pp}$ | 3.163 | 3.190 | 0.95% |

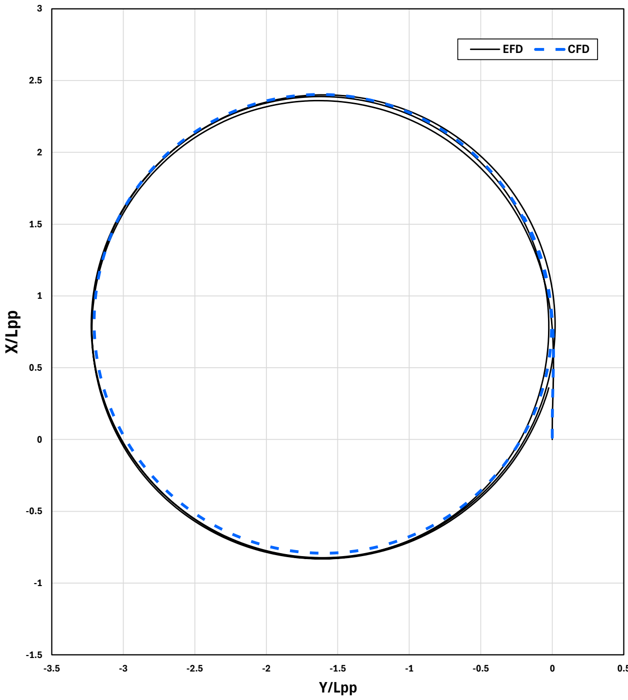


**Fig. 18.** Trajectories of the 35° Portside turning circle manoeuvre obtained from CFD and EFD

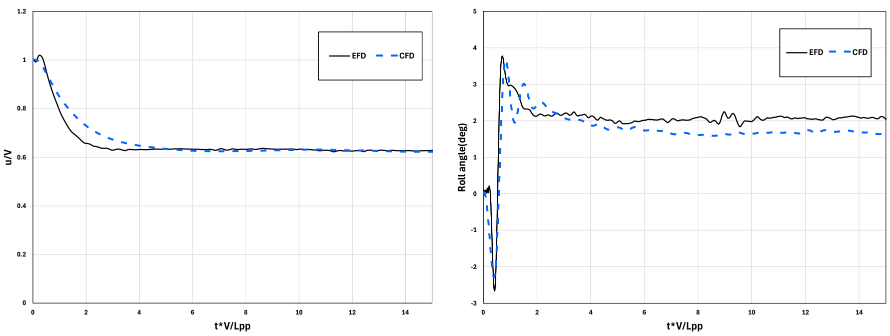


(a) Surge speed during the 35° Portside turning circle manoeuvre

(b) Roll angle during the 35° Portside turning circle manoeuvre

**Fig. 19.** Surge speed and roll angles during the 35° Portside turning circle manoeuvre

### 3.1.3. 20°/20° starboard side zigzag manoeuvre

The results comparing the heading angle and rudder angle from the CFD and EFD during the 20°/20° zigzag manoeuvre is presented in Fig. 20. As demonstrated in Fig. 20, the heading and rudder angles obtained from CFD are in good alignment with the results of EFD. For the results of surge speed and roll angle during the 20°/20° zigzag manoeuvre, they also correspond closely to EFD with only small discrepancies, as shown in Fig 21. In particular, the characteristics of the 20°/20° zigzag manoeuvre obtained from CFD and EFD are compared in Table 5. There are small differences between the results of CFD and EFD, but as mentioned earlier, the author believes that these differences do not affect the results of the present study.

**Table 5** Comparison of the 20°/20° the zigzag characteristics obtained from CFD and EFD

| | CFD | EFD (IIHR) | Difference |
|---|---|---|---|
| 1st overshoot angle (deg) | 25.66 | 25.68 | 0.15% |
| 2nd overshoot angle (deg) | 25.00 | 25.29 | 1.15% |

| | | | |
|---|---|---|---|
| 3rd overshoot angle (deg) | 24.90 | 25.30 | 1.60% |

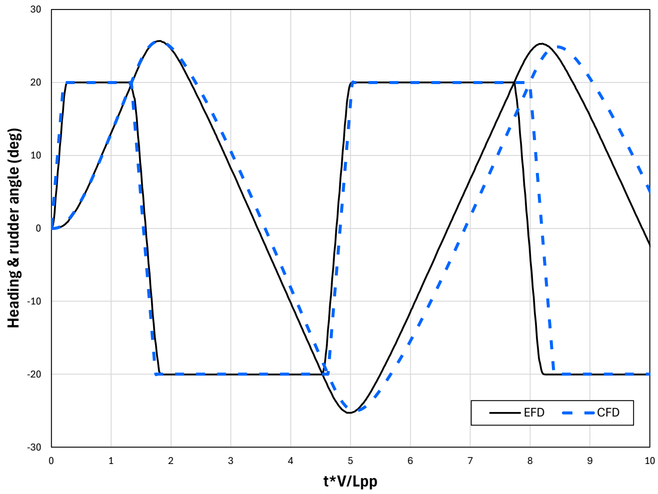


**Fig. 20.** Heading and rudder angle during the 20°/20° zigzag manoeuvre obtained from the CFD and EFD

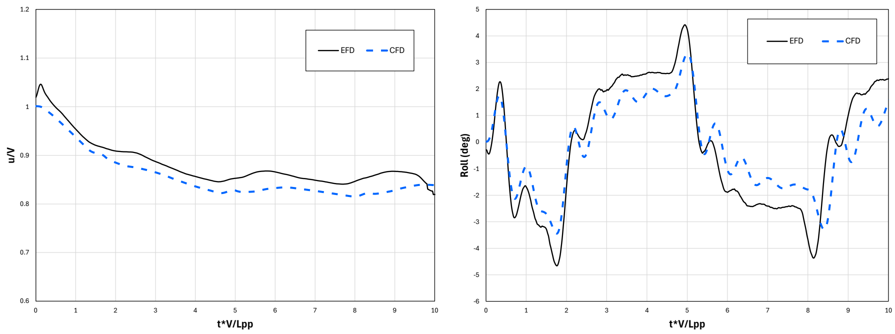


(a) Surge speed during the 20°/20° zigzag manoeuvre

(b) Roll angle during the 20°/20° zigzag manoeuvre

**Fig. 21.** Surge speed and roll angle during the 20°/20° zigzag manoeuvre obtained from the CFD and EFD

## 3.2. Uncertainty estimation

Similar to the validation studies, verification studies are also divided into two parts. The first part discusses the results of uncertainty estimation for the POW test simulations. The second part covers the part of uncertainty estimation for the free running simulations.

### 3.2.1. Uncertainty estimation of the POW test CFD model

To verify the results of POW test simulations, the spatial uncertainty for these simulations was estimated using the Grid Convergence Index (GCI) method (Celik et al., 2008). The verification tests were conducted in both forward and reverse rotating conditions for the propeller characteristics. Moreover, there were no available experimental data for the propeller characteristics under reverse rotating condition. Therefore, the results of the uncertainty test can confirm the results of the propeller characteristics under reverse rotating condition.

Table 6 and Table 7 present the discretization error in the spatial convergence test for open water test simulations under both forward and reverse rotating conditions. In both cases, uncertainty tests were conducted at an advance ratio of 1.0. As indicated in the tables, the uncertainties of the fine grid are below 1% in $K_T$, $10K_Q$, and $\eta_O$. The propeller open water curve for the reverse rotating propeller, used as input for the body-force propeller method in Push-Pull mode, is based on the results of the fine grid.

**Table 6** Discretization error in the spatial convergence test for forward rotating POW test simulations

| Spatial convergence test at J=1.0 | | No. Cells | $K_T$ | $10K_Q$ | $\eta_O$ |
|---|---|---|---|---|---|
| | Coarse | 1,670,858 | 2.81E-01 | 7.65E-01 | 5.84E-01 |
| | Medium | 2,165,336 | 2.97E-01 | 7.85E-01 | 6.02E-01 |
| | Fine | 3,397,855 | 2.98E-01 | 7.80E-01 | 6.07E-01 |
| | $GCI_{fine}$ | | 0.003% | 0.09% | 0.13% |

**Table 7** Discretization error in the spatial convergence test for reverse rotating POW test simulations

| Spatial convergence test at J=1.0 | | No. Cells | $K_T$ | $10K_Q$ | $\eta_O$ |
|---|---|---|---|---|---|
| | Coarse | 911,242 | 2.24E-01 | 6.94E-01 | 5.13E-01 |
| | Medium | 1,959,046 | 2.21E-01 | 6.70E-01 | 5.26E-01 |
| | Fine | 3,664,230 | 2.22E-01 | 6.74E-01 | 5.23E-01 |
| | $GCI_{fine}$ | | 0.02% | 0.30% | 0.36% |

### 3.2.2. Uncertainty estimation of the free running CFD model

The spatial and temporal uncertainties of the free running CFD model were also estimated using the GCI method (Celik et al., 2008). The uncertainty estimation was conducted for the 35° Portside turning circle manoeuvre simulation without using the Push-Pull mode. As presented in Table 8, the verification study evaluates the uncertainties of the simulations based on the lengths of advance, transfer, and the tactical diameter. As a result, these uncertainties are all below 1% in the turning circle characteristics. In this study, subsequent simulations with various Push-Pull mode conditions applied the fine grid and fine time step for each case.

**Table 8** Discretization error in the spatial and temporal convergence tests for free running manoeuvre simulations

| Spatial Convergence test | | No. Cells | Advance (m) | Transfer (m) | Tactical Diameter (m) |
|---|---|---|---|---|---|
| | Coarse | 1,112,239 | 7.50 | 3.60 | 10.39 |
| | Medium | 1,871,372 | 7.45 | 3.95 | 9.97 |
| | Fine | 3,408,819 | 7.43 | 3.96 | 9.96 |
| | $GCI_{fine}$ | | 0.46% | 0.01% | 0.02% |
| Temporal Convergence test | | $\Delta t$ (s) | Advance (m) | Transfer (m) | Tactical Diameter (m) |
| | | 0.08 s | 7.39 | 3.77 | 9.73 |
| | | 0.04 s | 7.42 | 3.93 | 9.94 |
| | | 0.02 s | 7.43 | 3.96 | 9.96 |
| | $GCI_{fine}$ | | 0.13% | 0.36% | 0.01% |

# 4. Results

## 4.1. Turning circle manoeuvre

The comparison of the trajectories of turning circle manoeuvres under various Push-Pull mode with those of the traditional turning method is shown in Fig. 22. As depicted in Fig. 22, the trajectories under symmetric rudder conditions exhibit a shrinking turning circle compared to the traditional turning method, regardless of whether the propeller is stopped or operating in reverse rotation. However, the trajectories under asymmetric rudder conditions rise above those of the traditional turning method. When comparing the trajectories based on propeller conditions, the trajectories of Push-Pull mode under reverse rotating propeller conditions show smaller lateral movement compared to those of the same rudder conditions in Push-Pull mode with the propeller off.

Moreover, manoeuvring performance in each Push-Pull mode is quantitatively evaluated in Table 8. As indicated in Table 8, without considering whether the propeller powers down or rotates in reverse, the symmetric rudder condition shows a decrease in the length of advance, transfer, and tactical diameter. Specifically, Push-Pull mode with symmetric rudder and reverse rotating propeller conditions shows reductions of 12.05% in advance, 38.63% in transfer, and 52.38% in tactical diameter, demonstrating the most improved manoeuvrability. On the other hand, Case 1, which has the off propeller condition with asymmetric rudder condition, shows an increase in advance, transfer, and tactical diameter. However, Case 3 which differs in propeller condition from Case 1 shows the same increasing trend in the length of advance, but a decrease in transfer and tactical diameter. Additionally, the different Push-Pull mode trajectories and the length of advance, transfer, and tactical diameter for each case can be seen in Fig. 23.

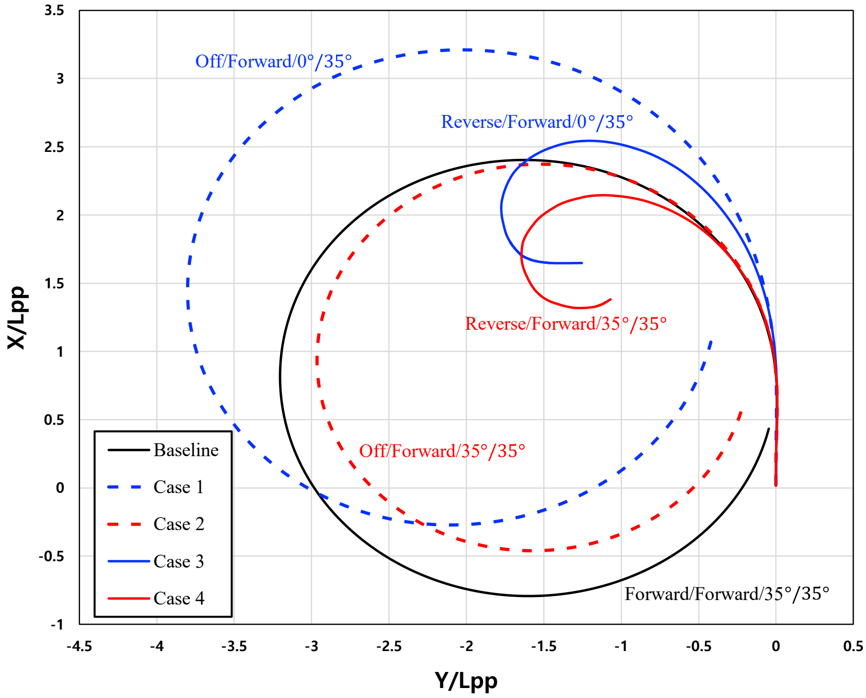


**Fig. 22.** Trajectories in Push-Pull mode under different conditions during turning circle manoeuvre

**Table 8** Variation in manoeuvring performance in each Push-Pull mode during turning circle manoeuvre

| | Advance | Transfer | Tactical diameter |
|---|---|---|---|
| Case 1 (Off/Fwd/0°/35°) | 34.26% | 30.57% | 13.89% |
| Case 2 (Off/Fwd/35°/35°) | -1.44% | -8.17% | -11.53% |
| Case 3 (Rev/Fwd/0°/35°) | 5.11% | -29.04% | -48.57% |
| Case 4 (Rev/Fwd/35°/35°) | -12.05% | -38.63% | -52.38% |

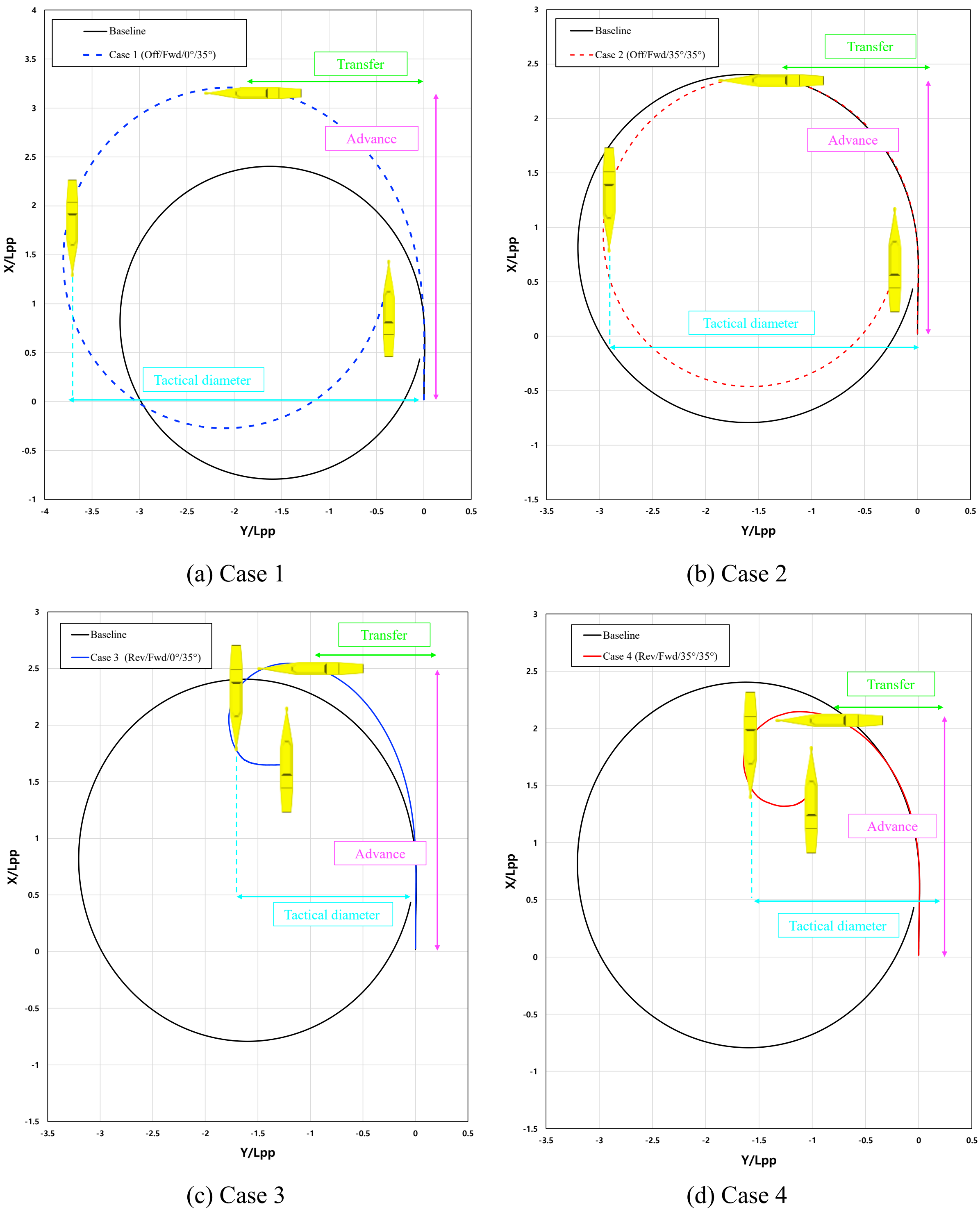


**Fig. 23.** Comparison of manoeuvrability characteristics in Push-Pull modes during turning circle manoeuvre

The comparison of surge speed and roll angle during the turning circle manoeuvre under each Push-Pull condition and traditional turning method is shown in Fig. 24 and Fig. 25. However, the time required for a 360° rotation of the heading angle differed for each case. Therefore, the operation time for each case was normalised using $T_c$, defined as the time spent for a 360° rotation of the heading angle. These times for each case are presented in Table 9. As illustrated in Fig. 24, all cases of the Push-Pull mode show a decrease in surge speed compared to Base case. Precisely, the Cases 3 and 4 which involve reverse rotating propeller conditions exhibit a significant decrease in surge speed with values approaching nearly zero. In the case of roll angle, Cases 1 and 2 show a similar trend to the Base case, with slightly smaller values. However, Cases 3 and 4 have smaller roll angles than the Base case, while exhibiting greater fluctuations.

In this context, the Push-Pull mode with a reverse rotating propeller condition significantly reduces the surge speed and results in a substantial decrease in the length of lateral movement. Moreover, longitudinal movements also decrease under the symmetric rudder condition with the propeller in reverse rotation. These reductions improve the performance of manoeuvrability. However, compared to the Push-Pull mode where the propeller is powered down in the reverse rotating configuration, the surge speed does not decrease as significantly. Therefore, the decrease in lateral movement is less pronounced. Nevertheless, lateral and longitudinal movements decrease under conditions where the propeller is powered down with a symmetric rudder. Conversely, under the same condition where the propeller is powered down, both lateral and longitudinal movements increase with an asymmetric rudder. This change results in a deterioration in the performance of manoeuvrability.

**Table 9** The time spent for 360° rotation of heading angle during turning circle manoeuvre, $T_c$

| | $T_c$ |
|---|---|
| Base (Fwd/Fwd/35°/35°) | 43.58 s |
| Case 1 (Off/Fwd/0°/35°) | 60.0 s |
| Case 2 (Off/Fwd/35°/35°) | 51.3 s |
| Case 3 (Rev/Fwd/0°/35°) | 73.2 s |
| Case 4 (Rev/Fwd/35°/35°) | 63.86 s |

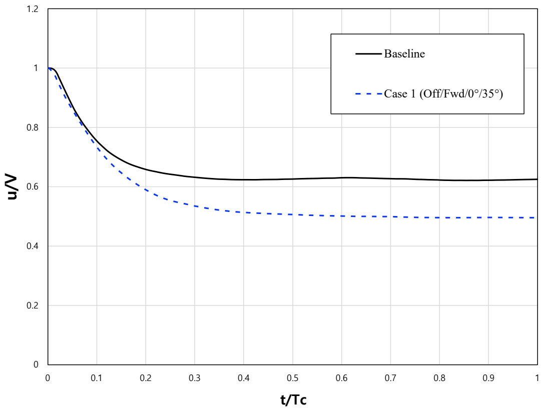


(a) Case 1

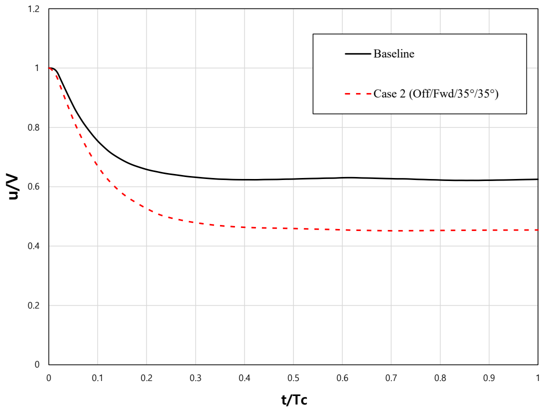


(b) Case 2

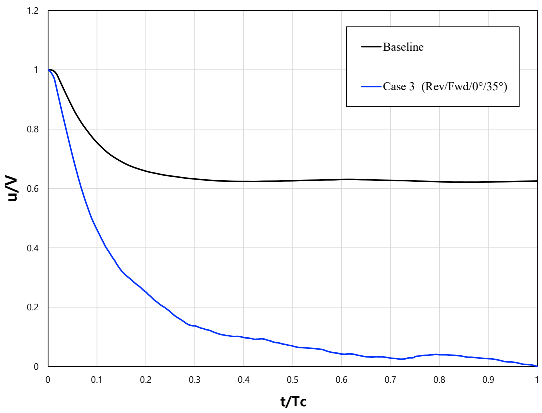


(c) Case 3

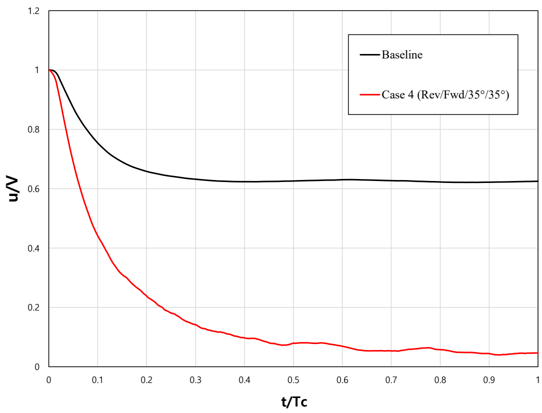


(d) Case 4

**Fig. 24.** Surge speed in Push-Pull mode under different conditions during turning circle manoeuvre

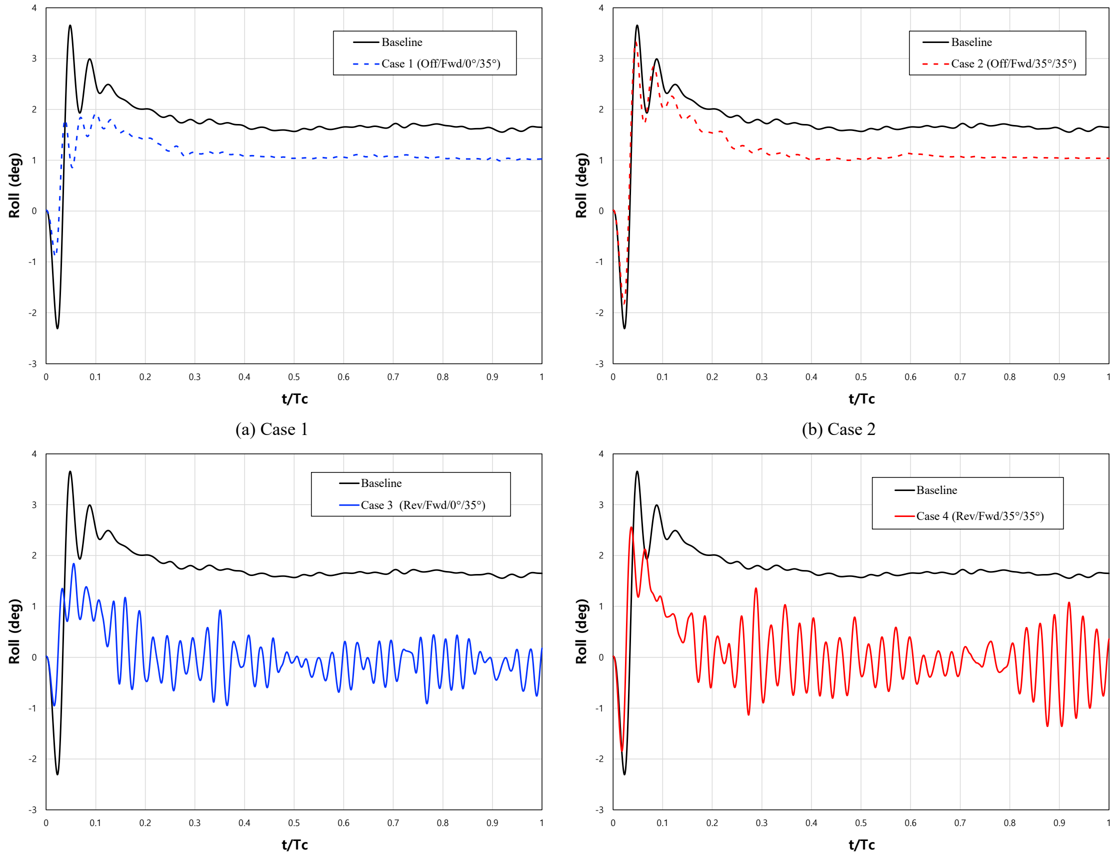


(a) Case 1 (b) Case 2

(c) Case 3 (d) Case 4

**Fig. 25.** Roll angle in Push-Pull mode under different conditions during turning circle manoeuvre

## 4.2. Turning back manoeuvre

The improvement of the turning circle manoeuvre when using the Push-Pull mode can be observed in Section 4.1. A key characteristic of the Push-Pull mode turning method is the reduction of lateral and longitudinal movements during operation. This characteristic can be notably seen in turning back manoeuvre (i.e. U-turn), which is closely related to actual operational conditions. Therefore, the variations of turning back manoeuvre were estimated in this section.

The trajectories in different Push-Pull modes during the turning back manoeuvre are presented in Fig. 26. The trend of trajectory variations when using the Push-Pull mode is the same as that observed during the turning circle manoeuvre. When using the Push-Pull mode with a symmetric rudder condition, the trajectories shrink compared to the base line, which represents the trajectory when using the rudder only. In the asymmetric rudder condition, the trajectories shift upwards and the length of longitudinal movement increases. A key point to note is that the lateral movement decreases when using the reverse rotating propeller condition, regardless of the rudder conditions.

Additionally, the variation of manoeuvring performance when using the Push-Pull modes is estimated in Table 11. Similar to the results of the turning circle manoeuvre, the manoeuvring performance improves when using the symmetric rudder condition, regardless of the propeller conditions. Specifically, the Push-Pull mode that uses reverse rotating propeller with a symmetric rudder shows the best improvement in estimation. On the other hand, the Push-Pull mode with an asymmetric rudder shows different results depending on the propeller conditions. For instance, when comparing Case 3 and Case 1, the length of longitudinal movements increases in both cases. However, the lateral movement decreases under the reverse rotating propeller condition, while it increases under the off propeller condition. Moreover, these variations in manoeuvring performance are illustrated in Fig. 27.

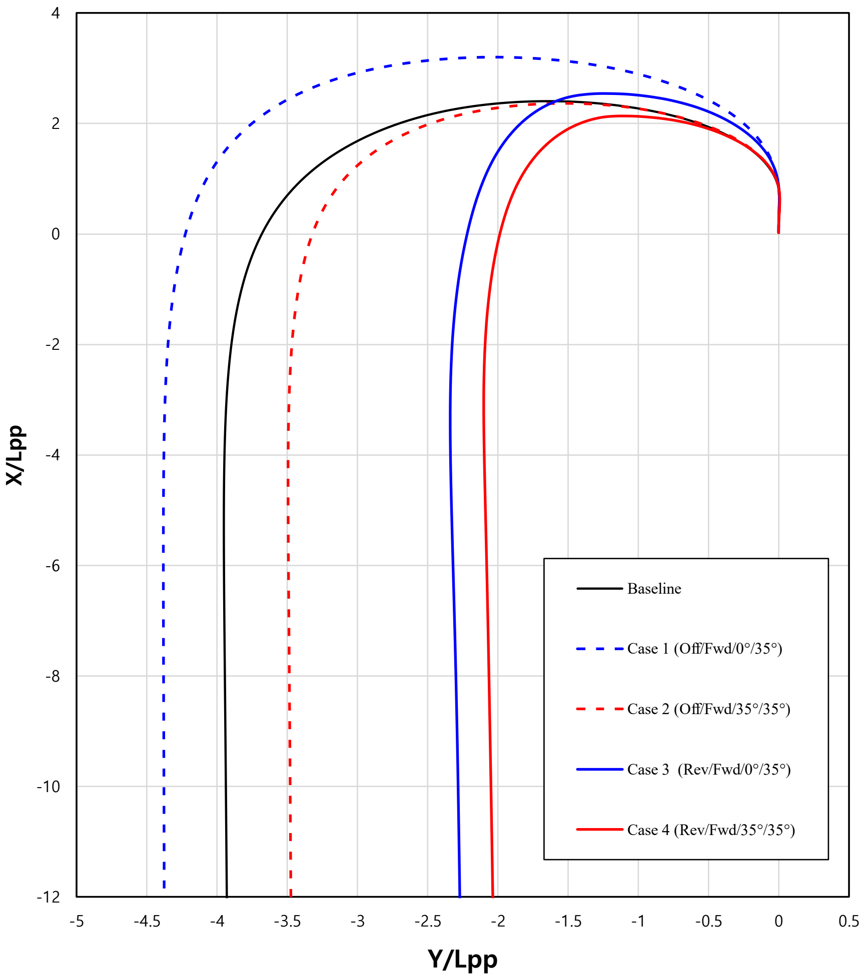


**Fig. 26.** Trajectories in Push-Pull mode under different conditions during turning back manoeuvre

**Table 11** Variation in manoeuvring performance in each Push-Pull mode during turning back manoeuvre

| | Advance | Transfer | Tactical diameter |
|---|---|---|---|
| Case 1 (Off/Fwd/0°/35°) | 33.85% | 28.86% | 11.47% |
| Case 2 (Off/Fwd/35°/35°) | -1.86% | -9.59% | -12.05% |
| Case 3 (Rev/Fwd/0°/35°) | 5.02% | -29.30% | -42.28% |
| Case 4 (Rev/Fwd/35°/35°) | -12.62% | -40.49% | -48.52% |

This is the author accepted manuscript of: Min, G., Choi, W., Yun, H., Kim, K., Terziev, M., Dai, D., Kim, D., & Song, S. (2025). Evaluation of Push-Pull manoeuvring mode for a naval ship using CFD. *Ocean Engineering*, *330*, Article 121143. https://doi.org/10.1016/j.oceaneng.2025.121143. For the purpose of open access, a CC BY 4.0 licence has been applied to this document.

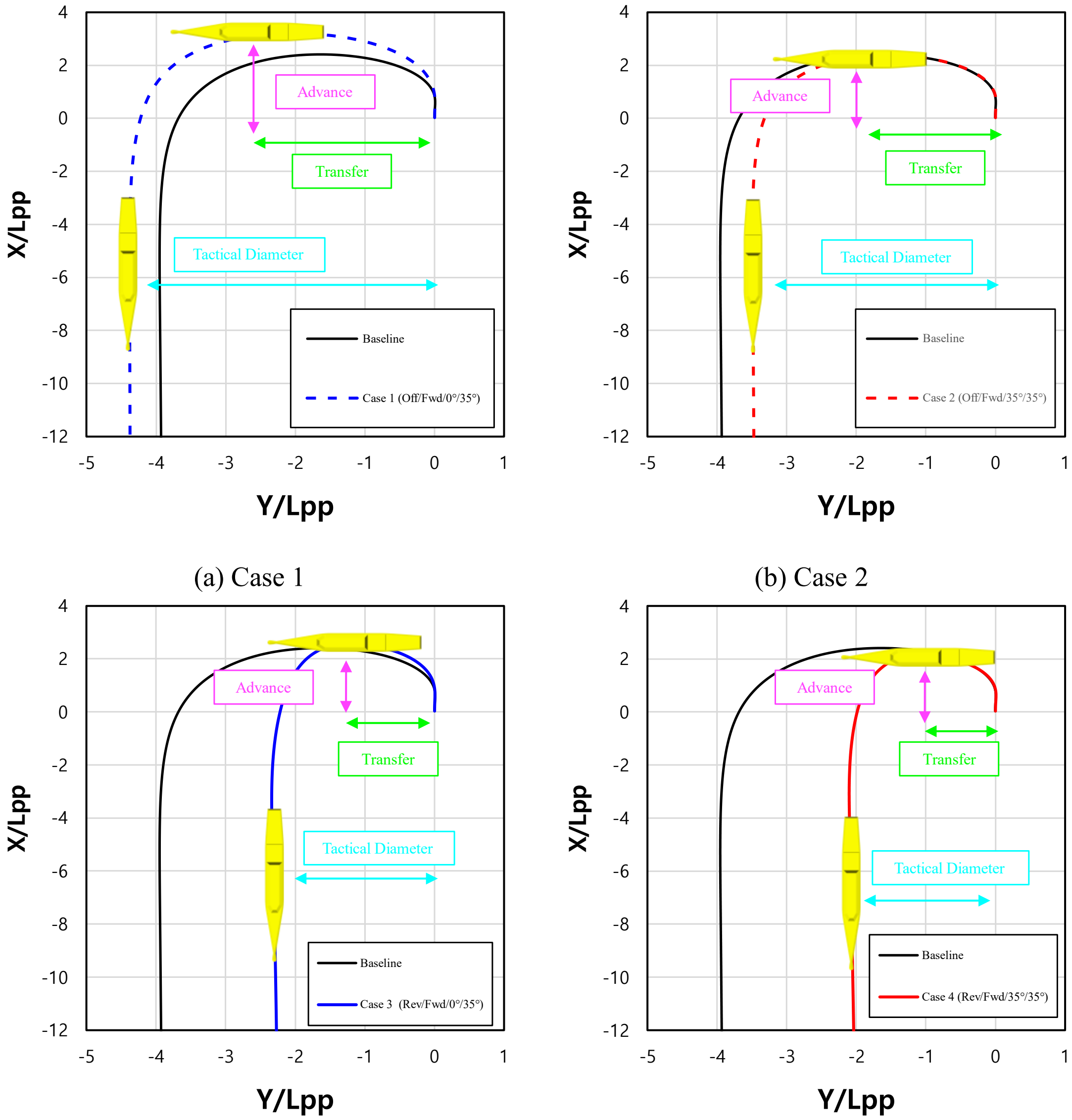


(a) Case 1 (b) Case 2

(c) Case 3 (d) Case 4

**Fig. 27.** Comparison of manoeuvrability characteristics in Push-Pull modes during turning back manoeuvre

As with turning circle manoeuvres, the time taken for a 180° rotation of heading angle during turning back manoeuvres is different in each case. Therefore, to compare the surge speed and roll angle between the Push-Pull modes and the Base case, the operation time is normalised. This is done by dividing the operation time by $T_u$, which is defined as the time taken for 180° rotation of heading angle during turning back manoeuvre. The value of $T_u$ for each case is indicated in Table. 12. In the perspective of surge speed, as shown in Fig. 28, surge speed decreases compared to the baseline when using the Push-Pull modes during operation. Specifically, the surge speed decreases significantly in the Cases 3 and 4 which have the reverse rotating propeller condition. On the other hand, the roll angle during operation also decreases compared to the baseline when using the Push-Pull modes, as presented in Fig. 29. However, fluctuations in the roll angle increase in the case of reverse rotating propeller condition.

These variations when using the Push-Pull mode in manoeuvring follow the same trend in both the turning circle manoeuvre and the turning back manoeuvre. Consequently, the Push-Pull mode with the reverse rotating propeller condition decreases lateral movements across both manoeuvres. Moreover, the Push-Pull mode with the symmetric rudder condition and reverse rotating propeller shows the best improvement in manoeuvring performance in both manoeuvres by reducing the lateral and longitudinal movements. However, the results of Push-Pull mode with off propeller condition differ depending on the rudder condition. With the symmetric rudder condition, manoeuvring performance improves, but it decreases with the asymmetric rudder. These results can answer the question that was previously raised regarding how applying the Push-Pull mode might affect the manoeuvring performance.

**Table 12** The time spent for 180° rotation of heading angle during turning back manoeuvre, $T_u$

| | $T_u$ |
|---|---|
| Base (Fwd/Fwd/35°/35°) | 54.82 s |
| Case 1 (Off/Fwd/0°/35°) | 71.56 s |
| Case 2 (Off/Fwd/35°/35°) | 70.0 s |
| Case 3 (Rev/Fwd/0°/35°) | 75.96 s |
| Case 4 (Rev/Fwd/35°/35°) | 72.04 s |

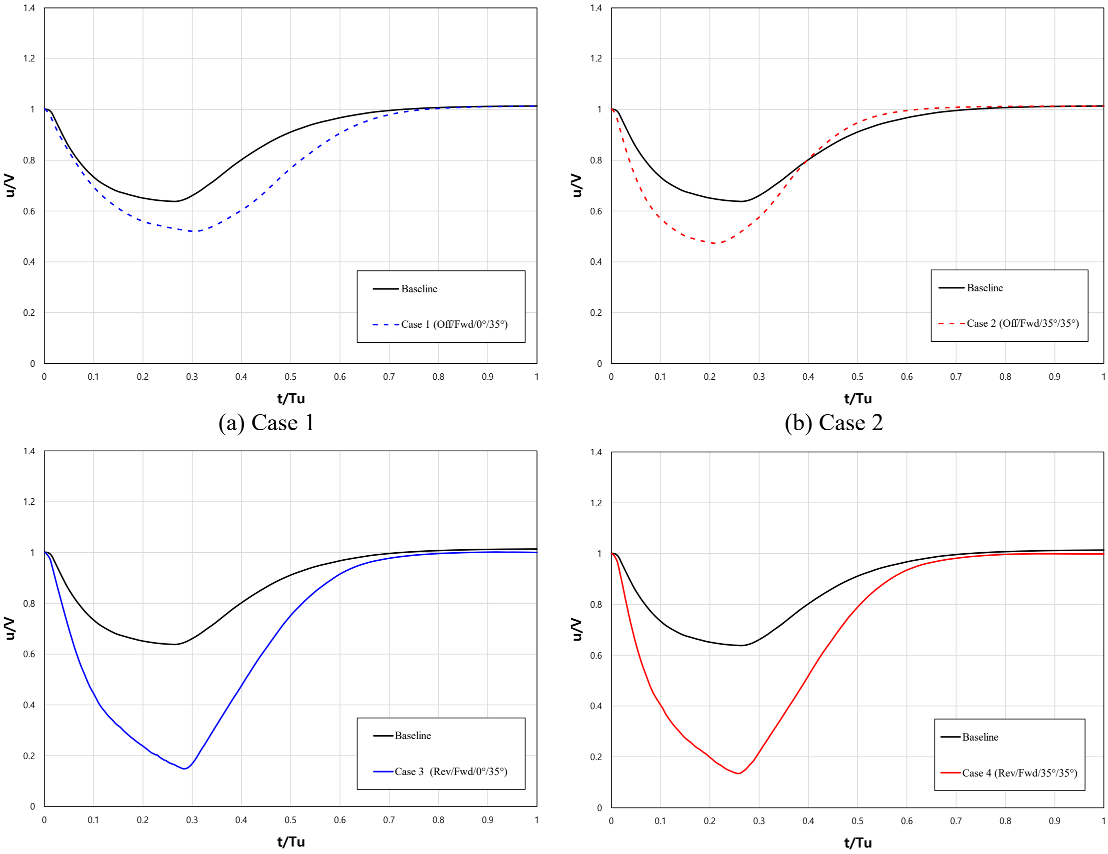


(a) Case 1

(b) Case 2

(c) Case 3

(d) Case 4

**Fig. 28.** Surge speed in Push-Pull mode under different conditions during turning back manoeuvre

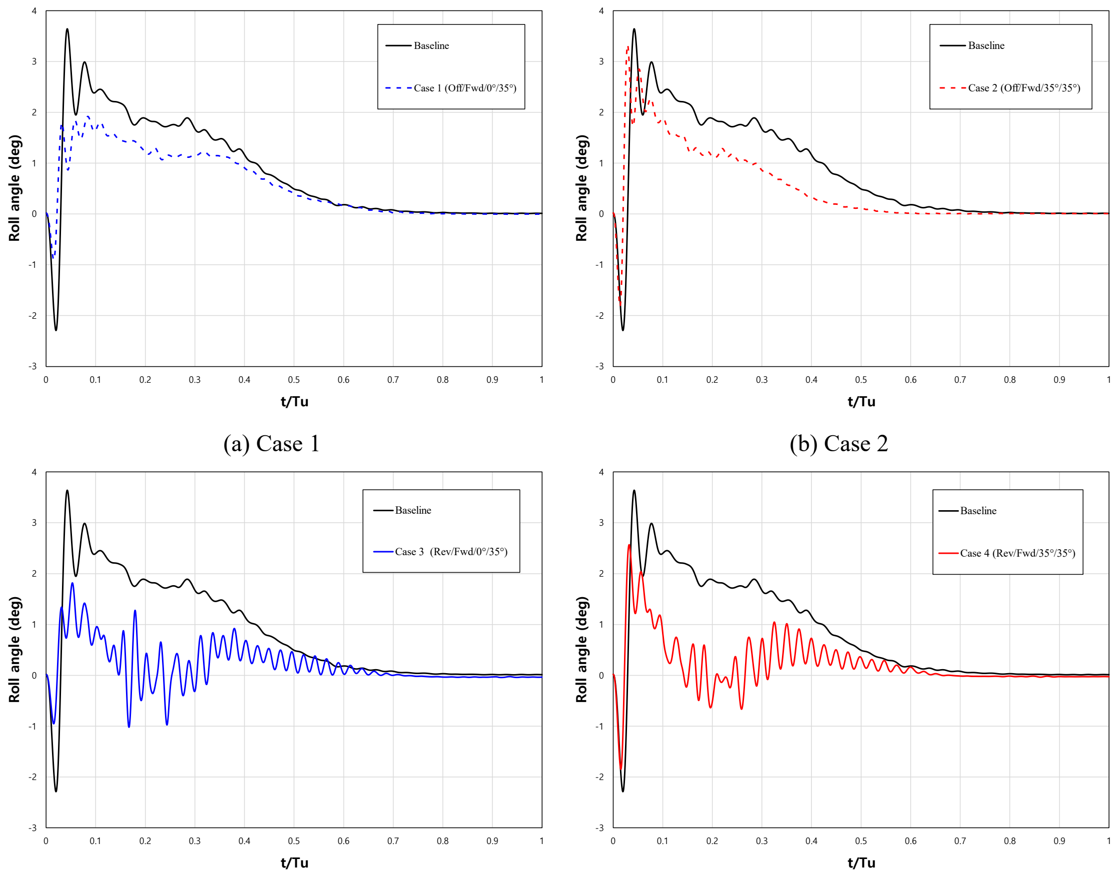


(a) Case 1 (b) Case 2

(c) Case 3 (d) Case 4

**Fig. 29.** Roll angle in Push-Pull mode under different conditions during turning back manoeuvre

## 5. Concluding remarks

In this study, a free running CFD model was developed for the ONRT model ship, which represents a naval ship. The simulation results were compared with the previous experimental results conducted by IIHR. Furthermore, their uncertainties were estimated through a verification study. In the simulations of the Push-Pull mode manoeuvre, the open water curve of the reverse rotating propeller obtained from the POW test simulations was applied. The results of POW test simulations for reverse rotating propeller were validated by the verification study due to the absence of experimental data.

The estimations of manoeuvring performance when using the Push-Pull mode are divided into two categories. The first category is the turning circle manoeuvre, and the second category is the turning back (i.e. U-turn) manoeuvre. In both manoeuvres, the conditions of the propeller and rudder are altered in four cases. These includes a reverse rotating or off propeller on the Portside, and a stationary or moving Portside rudder.

In the turning circle manoeuvre, the lateral movement decreased when using the Push-Pull modes with reverse rotating propeller. When using the Push-Pull mode with symmetric rudder and reverse rotating propeller, the greatest improvement in manoeuvring performance was observed. In this case, the length of advance, transfer, and tactical diameter decreased by 12.05%, 38.63%, and 52.38%, respectively. However, the variation in manoeuvring performance differed when using the Push-Pull modes with off propeller condition. In this case, the condition with symmetric rudder resulted in some improvement in manoeuvring performance. But the improvement was smaller compared to the same rudder condition with reverse rotating propeller. On the other hand, the Push-Pull mode with asymmetric rudder and off propeller condition led to decreased performance, as the length of advance, transfer, and tactical diameter increased.

The same results were observed in the turning back (i.e. U-turn) manoeuvre. The best improvement in manoeuvring performance was also observed when using the Push-Pull mode with symmetric rudder and reverse rotating propeller. Specifically, decreases were found in the length of advance, transfer, and tactical diameter by 12.62%, 40.49%, and 48.52%, respectively. Furthermore, the trend in other cases was noted to be identical during the turning circle manoeuvre.

These variations of trajectories under Push-Pull modes can be explained by the changes of surge speed and roll angle during the operation. When using the Push-Pull modes in the turning circle and turning back manoeuvre, the surge speed and roll angle of ship decreases during the operation. Particularly, the surge speed of ship decreases pronouncedly when applied the Push-Pull mode with reverse rotating propeller on manoeuvre. Therefore, this can lead to the significant decrease in the lateral movements.

In summary, we estimated the manoeuvring performance when the Push-Pull mode was applied to turning circle and turning back manoeuvres. As a result, using the Push-Pull mode with a reverse rotating propeller and symmetric rudder can improve performance in both manoeuvres. Based on this information, we hope that the manoeuvring performance of naval ships can be enhanced in operation. Lastly, the Push-Pull mode could be more effective at high speeds and during zigzag manoeuvres. Therefore, future research could focus on the variation in manoeuvring performance when the Push-Pull mode is used in high speed and zigzag manoeuvres.

## 6. References

Carrica, P. M., Mofidi, A., Eloot, K., & Delefortrie, G. (2016). Direct simulation and experimental study of zigzag maneuver of KCS in shallow water. *Ocean Engineering*, *112*, 117-133. https://doi.org/10.1016/j.oceaneng.2015.12.008

Celik, I. B., Ghia, U., Roache, P. J., & Freitas, C. J. (2008). Procedure for estimation and reporting of uncertainty due to discretization in CFD applications. *Journal of fluids Engineering-Transactions of the ASME*, *130*(7).

Dong, K., Yu, J., Liu, L., Zhang, D., & Wang, X. (2023). An investigation into the effects of damaged compartment on turning maneuvers using the free-running CFD method. *Ocean Engineering*, *271*. https://doi.org/10.1016/j.oceaneng.2023.113718

Ferziger, J. H., Perić, M., & Street, R. L. (2019). *Computational methods for fluid dynamics*. springer.

Hasanvand, A., Hajivand, A., & Ale ali, N. (2019). Investigating the effect of rudder profile on 6DOF ship turning performance. *Applied Ocean Research*, *92*. https://doi.org/10.1016/j.apor.2019.101918

Kim, D., Song, S., Sant, T., Demirel, Y. K., & Tezdogan, T. (2022). Nonlinear URANS model for evaluating course keeping and turning capabilities of a vessel with propulsion system failure in waves. *International Journal of Naval Architecture and Ocean Engineering*, *14*. https://doi.org/10.1016/j.ijnaoe.2021.11.008

Kim, D., Song, S., & Tezdogan, T. (2021). Free running CFD simulations to investigate ship manoeuvrability in waves. *Ocean Engineering*, *236*. https://doi.org/10.1016/j.oceaneng.2021.109567

Kim, D. J., Yun, K., Park, J.-Y., Yeo, D. J., & Kim, Y. G. (2019). Experimental investigation on turning characteristics of KVLCC2 tanker in regular waves. *Ocean Engineering*, *175*, 197-206. https://doi.org/10.1016/j.oceaneng.2019.02.011

Kim, I.-T., Kim, C., Kim, S.-H., Ko, D., Moon, S.-H., Park, H., Kwon, J., & Jin, B. (2021). Estimation of the manoeuvrability of the KVLCC2 in calm water using free running simulation based on CFD. *International Journal of Naval Architecture and Ocean Engineering*, *13*, 466-477.

Machado, L. d. V., & Fernandes, A. C. (2021). Proposals to Improve Load and Cavitation Computational Fluid Dynamics Analysis With Moving Reference Frame of a Conventional Propeller. *Journal of Offshore Mechanics and Arctic Engineering*, *143*(2). https://doi.org/10.1115/1.4048542

Park, J.-Y., & Kim, N. (2013). Modeling and controller design of crabbing motion for auto-berthing. *Journal of Ocean Engineering and Technology*, *27*(6), 56-64. https://doi.org/10.5574/ksoe.2013.27.6.056

Sanada, Y., Elshiekh, H., Toda, Y., & Stern, F. (2018). ONR Tumblehome course keeping and maneuvering in calm water and waves. *Journal of Marine Science and Technology*, *24*(3), 948-967. https://doi.org/10.1007/s00773-018-0598-3

Song, S., Demirel, Y. K., & Atlar, M. (2019). *An Investigation Into the Effect of Biofouling on Full-Scale Propeller Performance Using CFD* Volume 2: CFD and FSI,

Song, S., Demirel, Y. K., Atlar, M., & Shi, W. (2020). Prediction of the fouling penalty on the tidal turbine performance and development of its mitigation measures. *Applied Energy*, *276*. https://doi.org/10.1016/j.apenergy.2020.115498

Song, S., Kim, D., & Dai, S. (2024). CFD investigation into the effect of GM variations on ship manoeuvring characteristics. *Ocean Engineering*, *291*. https://doi.org/10.1016/j.oceaneng.2023.116472

Wang, J., & Wan, D. (2020). CFD study of ship stopping maneuver by overset grid technique. *Ocean Engineering*, *197*. https://doi.org/10.1016/j.oceaneng.2019.106895

Wang, J., Zou, L., & Wan, D. (2017). CFD simulations of free running ship under course keeping control. *Ocean Engineering*, *141*, 450-464. https://doi.org/10.1016/j.oceaneng.2017.06.052

Yasukawa, H., & Faizul, A. A. (2006). Experimental study on wave-induced motions and steady drift forces of an obliquely moving ship. *Journal of the Japan Society of Naval Architects and Ocean Engineers*, *3*, 133-138.

Yoo, W. J., Yoo, B. Y., & Rhee, K. P. (2006). An experimental study on the maneuvering characteristics of a twin propeller/twin rudder ship during berthing and unberthing. *Ships and Offshore Structures*, *1*(3), 191-198. https://doi.org/10.1533/saos.2006.0130

Yoshimura, Y., Ueno, M., & Tsukada, Y. (2008). Analysis of steady hydrodynamic force components and prediction of manoeuvring ship motion with KVLCC1, KVLCC2 and KCS. Workshop Proceedings of SIMMAN2008,